ELSEVIER

Contents lists available at ScienceDirect

Electrochimica Acta

journal homepage: www.journals.elsevier.com/electrochimica-acta



Degradation mechanisms of a proton exchange membrane water electrolyzer stack operating at high current densities

Benjamin Kimmel^a, Tobias Morawietz^{a,b}, Pawel Gazdzicki^a, Aldo S. Gago^{a,*}, K. Andreas Friedrich^{a,c}

- ^a Institute of Engineering Thermodynamics, German Aerospace Center (DLR), Pfaffenwaldring 38-40, Stuttgart 70569, Germany
- b Faculty of Science, Energy and Building Services, Esslingen University of Applied Sciences, Kanalstraße 33, Esslingen am Neckar 73728, Germany
- c Institute for Building Energetics, Thermotechnology and Energy Storage, University of Stuttgart, Keplerstraße 7, Stuttgart 70174, Germany

ARTICLE INFO

Keywords: PEM electrolysis Stack operation High current density Degradation Electrochemical and physical analysis

ABSTRACT

On the path to an emission free energy economy, proton exchange membrane water electrolysis (PEMWE) is a promising technology for a sustainable production of green hydrogen at high current densities and thus high production rates. Long lifetime, increasing the current density and the reduction of platinum group metal loadings are major challenges for a widespread implementation of PEMWE. In this context, this work investigates the aging of a PEMWE stack operating at 4 A cm⁻², which is twice the nominal current density of commercial electrolyzers. Specifically, an 8-cells PEMWE stack using catalyst coated membranes (CCMs) with different platinum group metal (PGM) loading was operated for 2200 h. To understand degradation phenomena, physical ex-situ analyses, such as scanning electron microscopy (SEM), atomic force microscopy (AFM) and X-ray photoelectron spectroscopy (XPS), were carried out. The same aging mechanism were observed in all cells, independent on their position in stack or the specific PGM loading of the membrane electrode assembly (CCM): (i) a decrease of ohmic resistance over time related to membrane thinning, (ii) a significant loss of ionomer at anodes, (iii) loss of noble metal from the electrodes leading to deposition of small Ir and Pt concentrations in the membrane, (iv) heterogeneous enrichment of Ti on the cathode side likely originating from the cathode-side of the Ti bipolar plates (BPPs). These results are in good agreement with the electrochemical performance loss. Thus, we were able to identify the degradation phenomena that dominate under high-current operation and their impact on performance.

1. Introduction

Climate change is one of the most pressing problems in our society. The increasing occurrence of heavy weather anomalies underlines the importance of reducing anthropogenic CO₂, which is one of the major greenhouse gases. This can only be achieved by shifting to renewable energy sources and a widespread expansion and implementation of renewable energy technologies. However, due to the weather-dependent fluctuation in renewable energy generation, like solar and wind energy, the importance of efficient and flexible energy storage and a resilience of the electrical grid is increasing rapidly, especially with growing shares of renewable energy in the electric supply [1]. Green hydrogen production is a promising option for chemical energy storage and transportation using excessive energy from renewable energy sources [2]. More important large quantities of hydrogen or its derivatives are required in

sectors like steel, chemical or fertilizer industries making the production of green hydrogen via electrolysis inevitable to decarbonize such industries [3,4]. Proton exchange membrane water electrolyzer (PEMWE) are highly suitable for direct coupling to renewable energy sources due to their rapid response time, wide operation range, high efficiency and power densities, compact design and outstanding gas quality [5–8]. However, ensuring long-term stability and reducing high capital costs are major challenges to surpass for a widespread implementation [9]. A good understanding of degradation phenomena is essential to ensure long lifetimes with cost-effective components. Therefore, degradation measurements have to be conducted although they are expensive and obviously require long-term experiments. Consequently, the development of accelerated stress test (AST) protocols is in the focus of the current research by academy and industry in particular [10,11]. Kuhnert et al. discussed various AST stressors and summarized recent studies on

E-mail address: aldo.gago@dlr.de (A.S. Gago).

^{*} Corresponding author.

ASTs with a focus on the CCM [12]. Such AST protocols consist of one or more stressor like high current density, overvoltage, high temperatures, high dynamic operation or differential pressures but the translation for accelerated degradation to nominal conditions is a challenge. Therefore, the identification of degradation mechanisms associated to these stressors is crucial. Reported degradation mechanisms for PEMWE are among others dissolution and leaching of catalysts and other metallic components [10,12-21], chemical membrane thinning, loss of mechanical stability, corrosion of porous transport layers (PTL) or bipolar plates (BPP) [10,12,16,19-24], hotspots [12,20,25] and mass transport issues [26,27]. Impurities can poison the catalyst coated membrane (CCM), affecting the conductivity of the membrane, deactivating the electrodes or even leading to pin holes, short circuiting the membrane [12,14,19-21,26-29]. However, a variety of electrochemical parameters and stressors can cause such degradation mechanisms in different manner and intensity. By using electrochemical in-situ and physical ex-situ analysis dominating degradation mechanisms for a specific stressor can be identified when applied separately. Such a differentiation contributes to a possible translation of accelerated degradation to nominal conditions. An overview on degradation of PEMWE is given by Feng et al. and the cause of degradation for the individual components is discussed [30].

Reducing capital cost of electrolysis systems can be achieved by either cheaper materials or by maximizing the current densities within acceptable ranges for efficiency and lifetime resulting in either lower required number of cells or greater hydrogen production rate [31,32]. However, the effect of higher current densities on the degradation behavior of electrolyzers needs to be understood in order to determine the sweet spot for higher production rates and accelerated degradation.

In this work, we investigated the degradation phenomena of a PEMWE-Stack, in particular of the CCMs with different loadings, under operation at 4 A cm⁻², which is twice the nominal operation of commercial electrolyzers [32–35] for almost 2200 h. In this study elevated current density was chosen as stressor to accelerate the degradation of the stack. At predefined time steps during operation the stack was electrochemical characterized using polarization curves and electrochemical impedance spectroscopy (EIS). Before and after operation the CCMs were analyzed by scanning electron microscopy (SEM) in combination with elementary analysis by energy-dispersive X-ray spectroscopy (EDX), X-ray photoelectron spectroscopy (XPS) and atomic force microscopy (AFM).

2. Experimental

2.1. Methodology

For this study an 8-cell short stack with an active area of 120 cm² was used. Two different types of CCMs were equipped. Cell 1 to 4 had a reduced total PGM loading (RL) of <2.4 mg cm⁻² and cell 5 to 8 had a standard loading (SL) of around 3–3.5 mg cm⁻². It is important to highlight that commercial PEMWE use high PGM loadings to ensure long lifetime like commercial CCMS with loadings ~3 mg cm⁻² [36] or reaching up to 10 mg cm⁻² like to one from Nel Hydrogen (formerly Proton Onsite) [37]. Confidentiality applies to some components of the used stack, so not all of them can be disclosed. The CCM consisted of Nafion™ N115CS membranes, Pt/C based cathode catalyst and Ir-based anode catalyst. The anode catalyst is known to be IrO₂ supported in TiO₂ (Elyst Ir75 0480 from Umicore, Germany). Uncoated Ti-BPPs with integrated flow field were used in combination with a carbon GDL on the cathode. The applied measurement protocol was designed as an AST using elevated current density as the stressor. Before applying the AST, 500 h of activation by applying different current densities from 0.1 A cm⁻² to 3 A cm⁻² was performed. Thereafter, a systematical characterization of the cells defined the initial performance and properties (T1). The characterization protocol consists of polarization curves (scanning rate 4 mA cm⁻² s⁻¹) at 30 °C and 55 °C up to 2 A cm⁻² and 4 A cm⁻²

respectively. Operation conditions and balance of plant (BoP) of the electrolyser system were as close as possible to the commercial systems, where there is a single flow on the anode side and not separate heating system to save cost. The operation temperature depends on the current density and feeding water acts as coolant. Therefore, deviations in temperature between different operation conditions are to be expected, such as during electrochemical impedance spectroscopy (EIS) or polarization curve measurements. EIS was performed at 0.25 A cm⁻² (amplitude of 3 A) and 26 °C by use of a Zahner electric IM6 at frequencies between 0.1 and 800 Hz for each of the 8 cells. To reach these currents a booster (Module PP240) was used enabling current densities up to 0.33 A cm⁻². In addition, EIS were performed for cell 2 and cell 5 at different current densities (0.025, 0.04, 0.08, 0.16, 0.25 and 0.33 A cm⁻²) to get detailed information of current-depending parameters. Those measurements were repeated after approx. 700 h at 4 A cm⁻² constant operation (T2) and after 2200 h (T4). At T3, after approx. 1400 h at 4 A cm⁻² only polarization curves were performed while at T4 additionally EIS was conducted to measure the temperature-dependency for Cell 2 and Cell 5 at 0.25 A cm⁻² for different temperatures (25, 32, 38 and 42 °C). The overall operation time including activation and characterization was approx. 3000 h. Fig. 1 summarizes the AST protocol. Panel a) and b) depicts the applied current density and the resulting stack voltage, respectively. It shows the activation period of 500 h as well as the characterization time steps presented as T1, T2, T3 and T4 before and after each AST part with approximately 700 h operation at 4 A cm⁻² for each.

At all-time steps (T1-T4) and before activation, samples of the ion exchange resin, which keeps the water resistivity above 10 M Ω , were collected and analyzed by XPS to quantify the accumulated ions. For the SEM, EDX and AFM analyses, pieces were cut out at three different positions (center, edge, and at intermediate) from the circular CCMs. For comparison pristine CCMs of both types were analyzed. After operation two cells with reduced loading (cell #2-R, cell #3-R), and one with standard loading (cell #8-S) were physically analyzed.

Cathodic cycling voltammetry (CV) measurements were conducted for the pristine, activated an operated CCMs following the JRC protocol to evaluate the loss of Pt [38]. For the measurements the upper limit was 500 mV and the lower limit 70 mV with a sweep rate of 20 mV s⁻¹ using the Zahner electric IM6 and the booster Module PP241. Electrochemical surface area (ECSA) of Pt without mass normalization was estimated by integrating the underpotential deposition of hydrogen peaks in a CV, corrected for the double-layer current, and using the charge density for a H monolayer and normalizing the cell area

2.2. Physical characterization

For investigation of the degradation phenomena the CCM samples were analyzed using SEM/EDX, AFM and XPS. Using SEM/EDX, the deposition of contaminants in the CCM as well as a reduction in thickness is detectable. Since the detection limit of EDX is in the range of 0.1 atomic percent, a detection of small amounts of contaminants is not possible; however, XPS exhibits sufficient sensitivity [39]. AFM can be used to investigate structure/material properties, and electronic as well as ionic conductivity. The material-sensitive measurements, where topography is evaluated together with mapping of different mechanical and surface properties, allow the discrimination between ionomer and noble metals or carbon components [21]. In combination with current measurements and local V(i) curves ionomer coverage of Ir-catalysts was determined and the fraction of conductive electrode area before and after operation was analyzed [10,40,41]

2.2.1. Atomic force microscopy

For atomic force microscopy (AFM) analysis, cross-sections of the samples were cut with a glass knife by microtome (Leitz, Germany). The samples were fixed with conductive tape on an AFM steel disc. With a Bruker Multimode 8, the AFM analysis was performed using

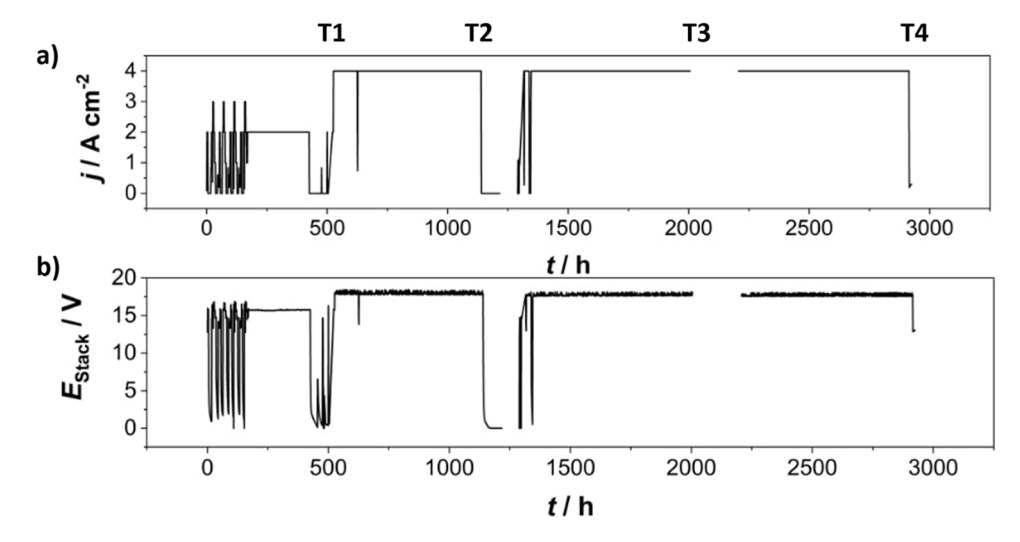


Fig. 1. a) Applied protocol including the activation and the AST parts and the b) voltage response of the stack.

Quantitative Nanoscale Mechanical Mapping mode (QNM), conductive tapping (TUNA), and kelvin probe force microscopy (KPFM). QNM mappings of adhesion force, stiffness (DMT modulus) and deformation were performed simultaneously with height measurements. PPP-NCH-Pt tips (42 N/m; Nanosensors) were used for measurement of the electronic current. For all current measurements of the electrodes the BIAS voltage was set to 1 V (tip at ground). The evaluation of the conductive area of the electrodes was performed by surface fraction analysis of the current image mapping while all positive currents were counted. For calculation of the mean conductive area fraction, always three different areas of $3\times 3~\mu m^2$ of the pristine and operated samples were measured with conductive tapping mode.

For KPFM measurements PFQNE-Al tips (0.8 N $\rm m^{-1}$; Bruker) were used keeping a lift height of 115 nm above the sample surface. All measurements were performed in an environmental chamber at a controlled relative humidity of 60 %. Further details on the measurements can be found in references [42].

2.2.2. X-ray photoelectron spectroscopy

The X-ray photoelectron spectroscopy (XPS) measurements were performed with a Thermo Scientific ESCALAB 250 ultra-high vacuum facility. For the XPS measurements the cross-sections were cut inclined to enlarge membrane surface due to the relatively large X-ray spot size and detection sensitivity.

2.2.3. Scanning electron microscopy/energy dispersive X-ray system

Scanning electron microscopy (SEM) of the CCMs was performed with a JEOL JSM-7200F, combined with Bruker Quantax energy dispersive X-ray analysis system (EDX). In addition to the analysis of the surface, cross-sections of the CCMs are required. For SEM/EDX analysis the CCM samples were cleaved in liquid nitrogen. EDX analysis of the electrodes was performed with 15 kV excitation energy and a high probe current for two minutes. For cross-sections with the glass knife the samples were embedded with Araldite 502 epoxy resin (SPI-Chem).

3. Result and discussion

The analysis of the degradation phenomena of the 8-cell stack using an AST protocol was carried out as follow:

- i. Beginning of Test (BoT) characterization of the stack and CCMs (electrochemical) and physical analysis of reference components.
- Electrochemical characterization at given time steps: including polarization curves and EIS measurements.

 End of Test (EoT) characterization using AFM, SEM/EDX, and XPS.

3.1. Electrochemical analysis

Fig. 2a) and b) shows BoT polarization curves from 0 to 2 A cm⁻² and from 0 to 4 A cm⁻², respectively. It clearly shows the effect of the reduced PGM loading for cell 1 to 4, which exhibit increased cell voltages. This can be explained from the results of EIS measurements as shown in Fig. 2c). Cell 1 to 4 show mainly an increased ohmic resistance determined by the high frequency resistance (HFR) as the first intersection of the x-axis in the Nyquist diagram. It can be concluded, that higher PGM loading improves the contact resistance resulting in lower HFR lower potentials.

The second intersection in Fig. 2c) represents the overall resistances of the cell as the low-frequency-resistance (LFR). Cells using the same CCM, namely cell 1 to 4 and cell 5 to 8 show very similar performances and only small deviations in the HFR and LFR. The cells show very similar and comparably performance, only cell 6 showed a slightly higher ohmic resistance and therefore worse performance. Irregularities during the assembly of the stack can influence the contact resistance between the components. While this cannot be directly confirmed, it still represents a coherent reason for the measured discrepancies. Importantly, this does not influence the following analysis and conclusions.

Measurements and analysis at the different time steps (T1 to T4) enable the possibility to investigate the degradation of the cells during the course of the experiment. For better visibility and comparability, the average values of the cells of each type were used in the plots. The average value of cell 1 to 4 is labeled as RL while the average value cell 5 to 8 is labeled with SL. A comparison of the different timesteps is shown in Fig. 3. The polarization curves for all cells and time steps are displayed in the supplementary information (SI) in Fig. S1.

The polarization curves in Fig. 3a) slightly increases in performances after the 2200 h operation (T4). The detailed view of the area of higher current density in Fig. 3b) reveal that in fact an improvement in performance was measured for SL as well as for RL. This aligns well with the EIS measurements in Fig. 3c). Only at T4 we observed a slight decrease in performance in the polarization curve compared to the previous step, which might be related with moderate mass transport contributions. Nevertheless, for each step in the EIS a reduction in the HFR and the LFR is visible. Since the width of the arcs are roughly in the same order of magnitude it can be concluded that the reduced HFR is mainly responsible for the performance improvement over time.

To investigate this phenomenon the HFR and LFR were evaluated for

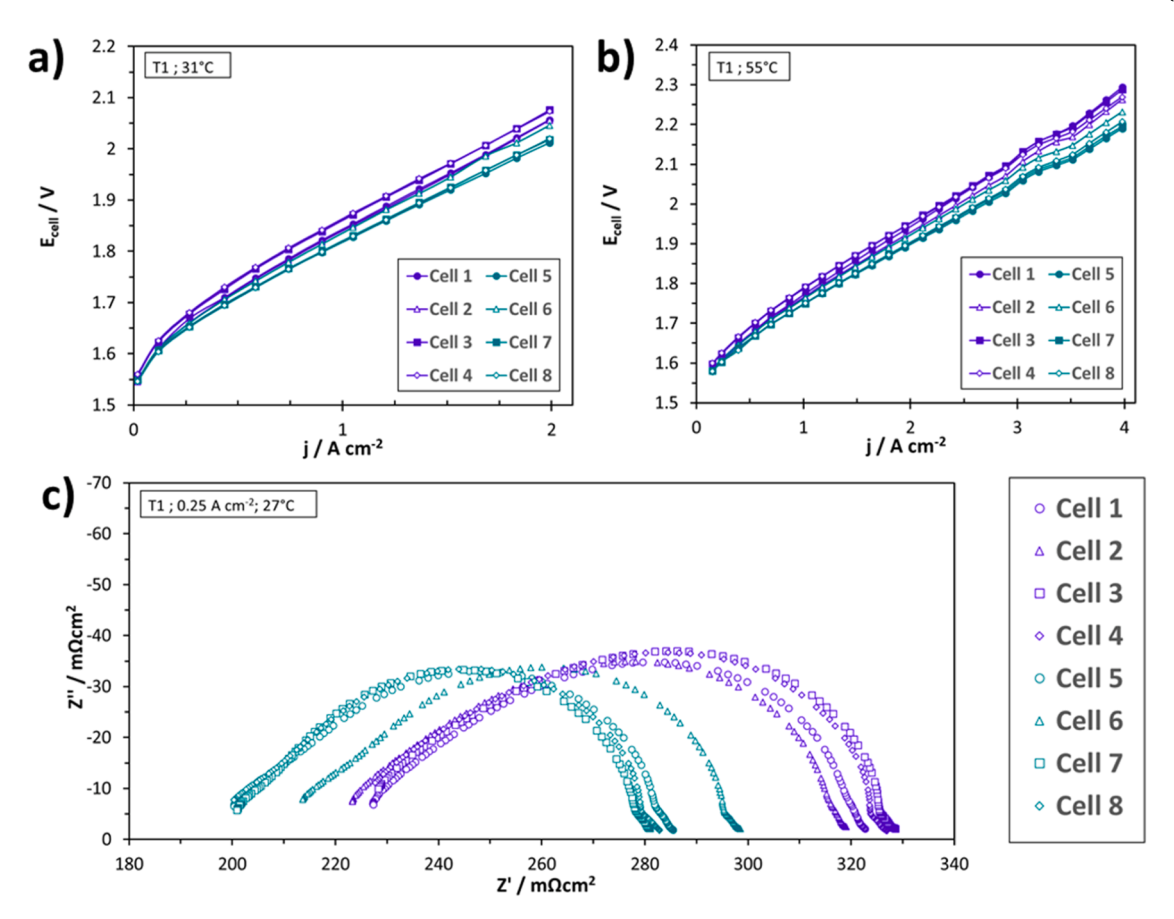


Fig. 2. Characterization of the different cells in the stack at T1. a) and b) shows the polarization curves up to 2 A cm⁻² and 4 A cm⁻² respectively. c) EIS measurements at 0.25 A cm⁻².

all cells in the stack at different time steps in Fig. 4. In addition, the HFR and LFR were determined for different current densities as well. For this investigation cell 2 and cell 5 were chosen exemplary for RL and SL respectively. The values for HFR and LFR were determined using EIS measurements, plotted in SI Fig. S2 and Fig. S3.

Fig. 4a) compares the HFR of cell 2 and cell 5 at different current densities for T1 and T4. Clearly, the HFR reduced significantly during operation for all current densities and all cells no matter if they have standard or reduced loading. Also, a reduction in the LFR was observed for cell 2 and cell 5 shown in Fig. 4b) with higher magnitude at lower current densities. The reduction in HFR and LFR for all cells at 0.25 A cm⁻² is plotted in Fig. 4c) and d) respectively. It can be observed that the HFR reduction is in similar ranges for all cells regardless of whether type of CCM (SL & RL) or current densities it is. In contrast the LFR showing a strong current dependency which higher values at low current densities. This leads to the effect, that the impact of the HFR reduction on the overall performance increases significantly at higher current densities. Absolute and normalized reduction values as well as the ratio of HFR/ LFR are shown in SI Table S1 and Table S2.

Fig. 5a) showing the current-dependency of HFR, LRF and cell potential. Up to $0.33~{\rm A~cm^{-2}}$ HFR remains stable, while LFR drops significantly by about 3 times. This aligns with the increasing ration of HFR/LFR. The cell potential rises continuously but with a progressively decreasing gradient. Changes in temperature have mainly an impact on the HFR, whether for SL or RL, displayed in Fig. 5b) observed by the similar slope of HFR and LFR.

CV measurements were conducted to investigate possible Pt losses during operation. Fig. 6 shows the results for the pristine, activate and operated CCMs for the standard loading in Fig. 6a) and the reduced loading in Fig. 6b). It can be clearly seen that Pt loss occurred noticeably for both. The ECSA in Fig. 6c) confirms this loss in Pt catalyst, which was

more pronounced for the reduced loaded CCM.

3.2. Physical ex-situ analysis

Various physical ex-situ methods were used to investigate the degradation phenomena of the CCMs after operation. For these analyses, cells close to the endplates were chosen, namely cell 2 and cell 8, while cell 3 represents a more centrally located cell. The cells were analyzed at different positions as well as reference CCMs for SL and RL for comparison.

The topography and electronic current mappings of the anode of cell 2 and the reference of the reduced loaded CCMs are shown in Fig. 7. After operation, the conductive area fraction increased significantly. The lighter color in Fig 7b) and d) indicates greater conductivity while darker areas correlate with lower conductivity up to complete nonconductivity in the black areas. Such changes in conductivity especially after high current operation are typical for changes in catalyst and ionomer occurrence at the surface impacted by dissolution and redeposition [10,19,24,43]. Therefore, the larger conductive areas reflect sections with reduced ionomer and higher amount of Ir-oxide catalyst particles. Changes in the height structure of the surface visualized in Fig. 7a) and c) confirm this assumption.

To quantify the change in conductivity the average electronically conductive area fractions on the anode side at different positions was determined for cell 2, cell 3 and cell 8 and compared with pristine reference samples shown in Fig. 8.

The conductive area fraction of the reduced loaded reference anode was slightly higher than for the standard noble metal loaded reference anode. After operation, the conductive area fraction of all anodes was generally higher with the exception of the edge position of cell 3 and cell 8, where no change occurred. At closer view, similar behaviour occurred

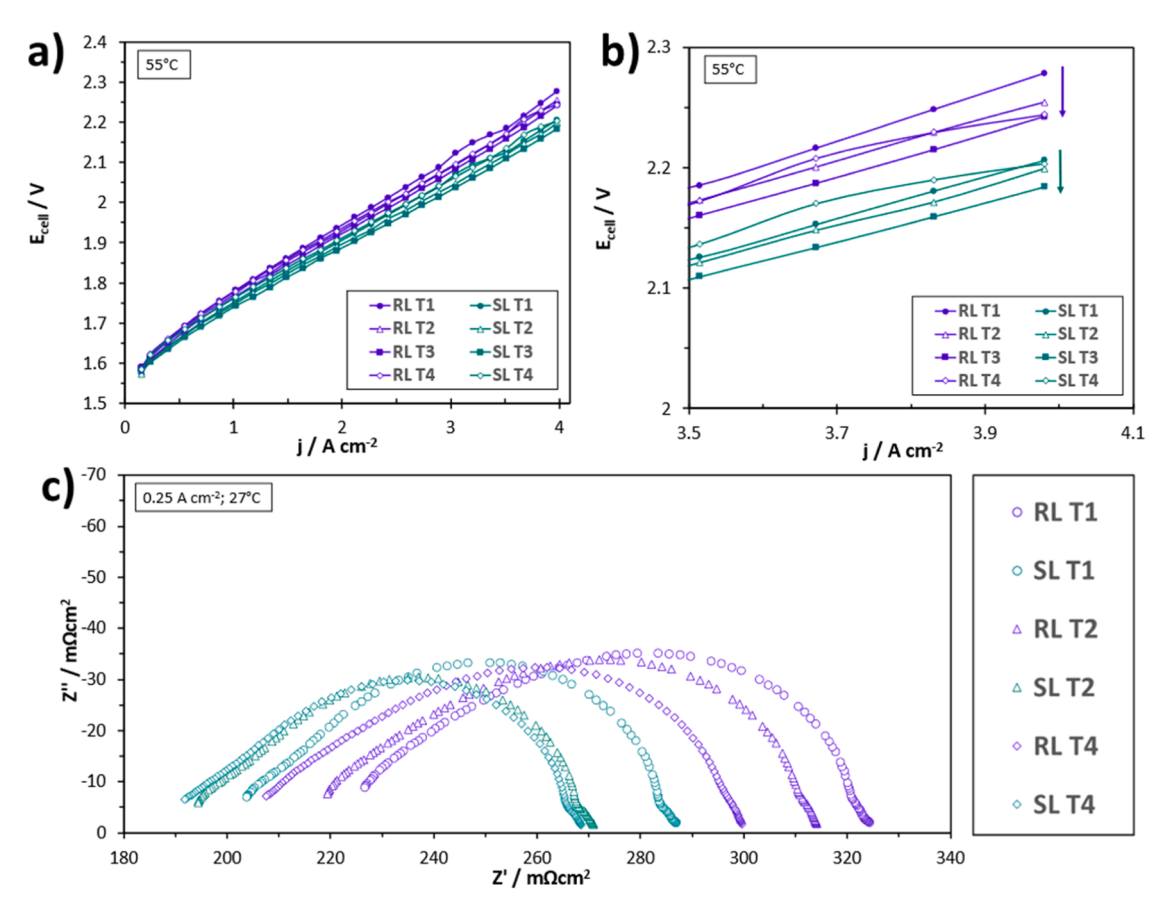


Fig. 3. Average values of cell 1 to 4 (RL) and averages values of cell 5 to 8 (SL) were calculated to plot the a) polarization curves at the time steps T1 to T4 and b) a detailed view of the polarization curves of the area of higher current density. c) shows the EIS measurements at 0.25 A cm⁻² at T1, T2 and T4.

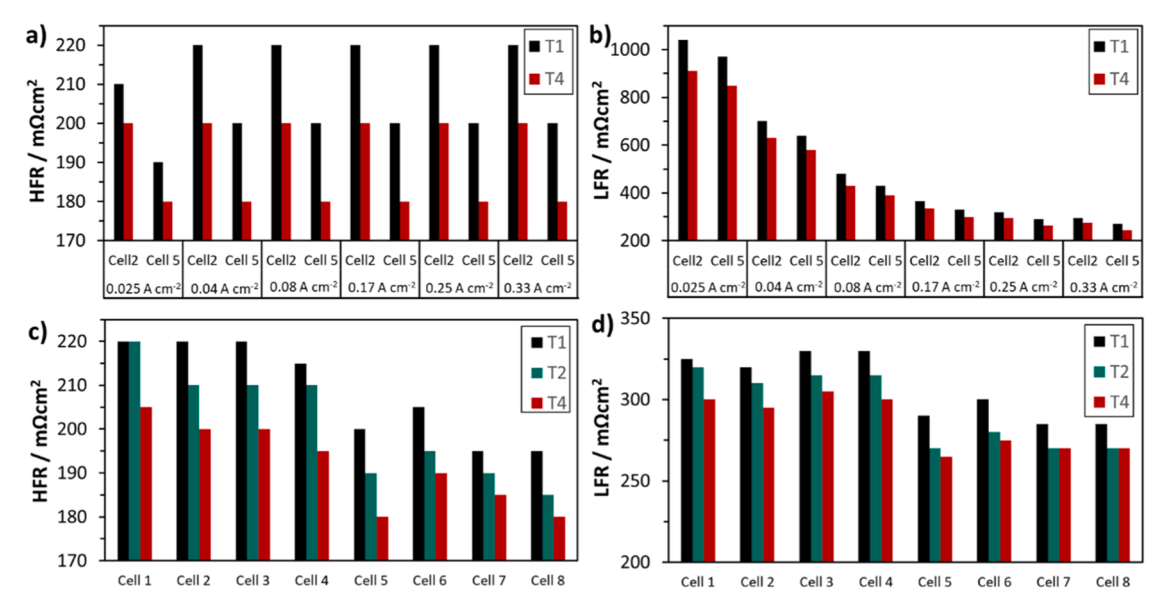


Fig. 4. a) HFR and b) LFR for cell 2 and cell 5 for different current densities and time steps. c) HFR and d) LFR for cell 1 to 8 for different time steps (T1, T2 and T4).

at the different positions of cell 3 and cell 8, where the conductive area was highest at the intermediate position. In contrast cell 2 deviates from this trend showing the smallest conductive area fraction at intermediate position. Possible reasons for such an increase in conductive area fraction after operation are the loss of ionomer or of the $\rm TiO_2$ support as well as the formation of agglomerations leading to more exposed iridium which is most likely due to the observed changes in height structure and

conductivity in Fig. 7. The increase in conductive area fraction was detected for both SL and RL, but no trend related to the position was observed.

In contrast a reduction of conductive area fraction over time was observed for the cathode side of cell 2, cell 3 and cell 8 in Fig. 9.

Again, the conductive area fraction of all cells are higher for RL than for SL and a clear reduction after operation could be observed. Cell 3 and

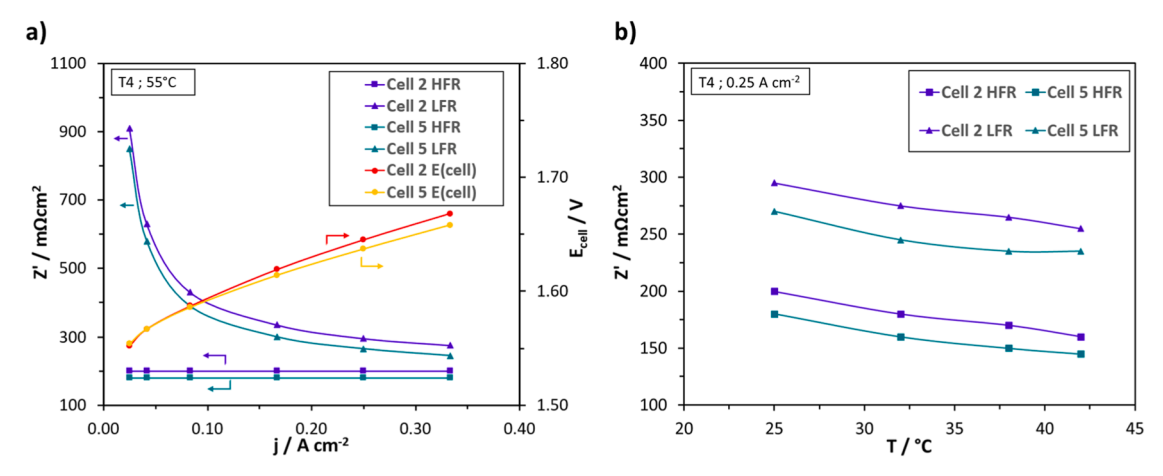


Fig. 5. a) Current-dependency of HFR, LFR and cell potential for cell 2 and cell 5 at T4. b) temperature-dependency of HFR and LFR at 0.25 A cm⁻² at T4.

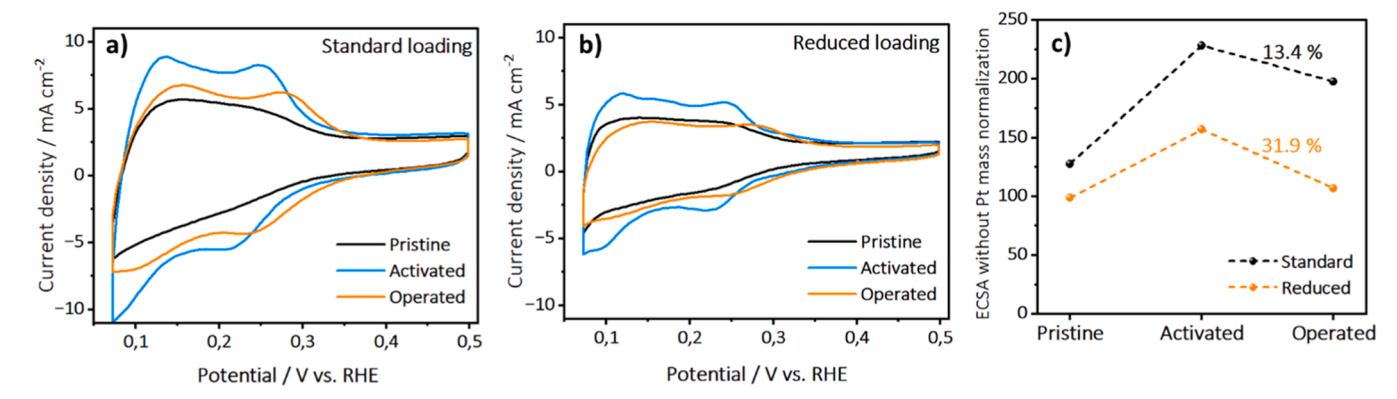


Fig. 6. CV measurements of the pristine, activate and operated CCMs for a) standard loading (cell 8), b) reduced loading (cell 2) and in c) the ECSA for both standard and reduced loading.

cell 8 had the highest conductive area reduction at the edge positions followed by slightly less conductivity at intermediate position and lowest values at the center. Cell 2 showed the highest reduction of conductive at the center position and almost no change at the edge. In general, the reduction of conductive area fraction was in similar ranges for the standard Pt loaded cathode (cell 8) and the reduced loading (cell 2 & 3). Such a decrease of electronically conductive area fraction at the cathode can be explained by either a loss of Pt catalyst or the deposition of less conductive contaminations. The ECSA in Fig. 6 already revealed a loss in Pt for both the standard and the reduced loading.

By EDX analysis a decrease of Ti on the anode side as well as a noticeable increase of Ti on the cathode side was detected. Fig S4 show the anodic and cathodic EDX-spectra highlighting the changes in Ti.

In Fig. 10a) and d), the SEM images provide an overview of the cathode surfaces of cell 2 and cell 8, respectively, revealing a spot-like appearance. By EDX analysis, these spots were identified as Ti depositions on the cathode surfaces revealing an inhomogeneous distribution of Ti contamination. An enrichment of Ti in the cathodes after operation was also reported in previous work [21,26]. In Fig. 10b), a higher magnification of two spots of cell 8 is presented. The dark spots are Ti and oxygen-rich areas on the cathode and therefore appear darker than the surrounding Pt-rich electrode surface. EDX derived Ti mappings of the cathode surface of cell 8 and cell 2 are overlaid on the SEM images in Fig. 10c) and e), respectively. The occurrence of Ti and oxygen rich areas is in good agreement with the observed reduction in conductive fraction in Fig. 9. In the CCM cross-section in Fig. 10e), one of the Ti-rich areas at the edge is cut through. At this position a high concentration of Ti is also present in the cathode layer below the surface. Below the Pt-rich areas no Ti is present in the cathode layer. In Fig. 10f) it is visible

that the Ti likely has penetrated the cathode from above. At positions with highly enriched Ti still Ti-free areas are visible at the interface to the membrane. In combination with the spotted distribution of Ti in the cathode, this indicates that the source of Ti is probably at the cathode side; an origin from the anode is expected to result in a more homogeneous Ti distribution at the cathode. With EDX analysis no Ti could be detected in the membrane (Fig. 10f), a fact that also points to a cathode-side origin of the Ti. Uncoated Ti components or defects in the coating were found to be possible sources for Ti contamination in previous work [21,26]. Known degradation phenomena include hydrogen uptake and embrittlement, which lead to the release and dissolution of Ti ions that contaminate and inhibit the catalyst surface [44–47].

A minor diffusion below the detection limit of EDX of Ti from the anode through the membrane cannot be excluded but is unlikely to solely explain the massive Ti content at the cathode side. The EDX spectra for cell 8 are shown in SI Fig. S5.

In Fig. 11, the cross-section of cell 2 (Fig. 11a) and the EDX spectra (Fig. 11b) recorded at the marked positions in the anode and in the membrane is exhibited. While distinct peaks from the Ti content are present in the red spectrum of the anode, no peaks are detectable in the green and blue spectra from the membrane. Radousky et al., who observed Ti enrichment at the cathode, concluded that in their system the source of Ti was the uncoated titanium porous transport layer at the anode [26,48]. Although the findings and observations in this study suggest that the cathode side is the source of Ti, it cannot be completely ruled out that the anode side may also be a potential source of Ti. Due to the following reasons the cathode side is in this work likely the source of Ti: (i) detection of larger spot-like areas on the cathode whereas a Ti ion stream from the anode would lead to a more homogeneous distribution

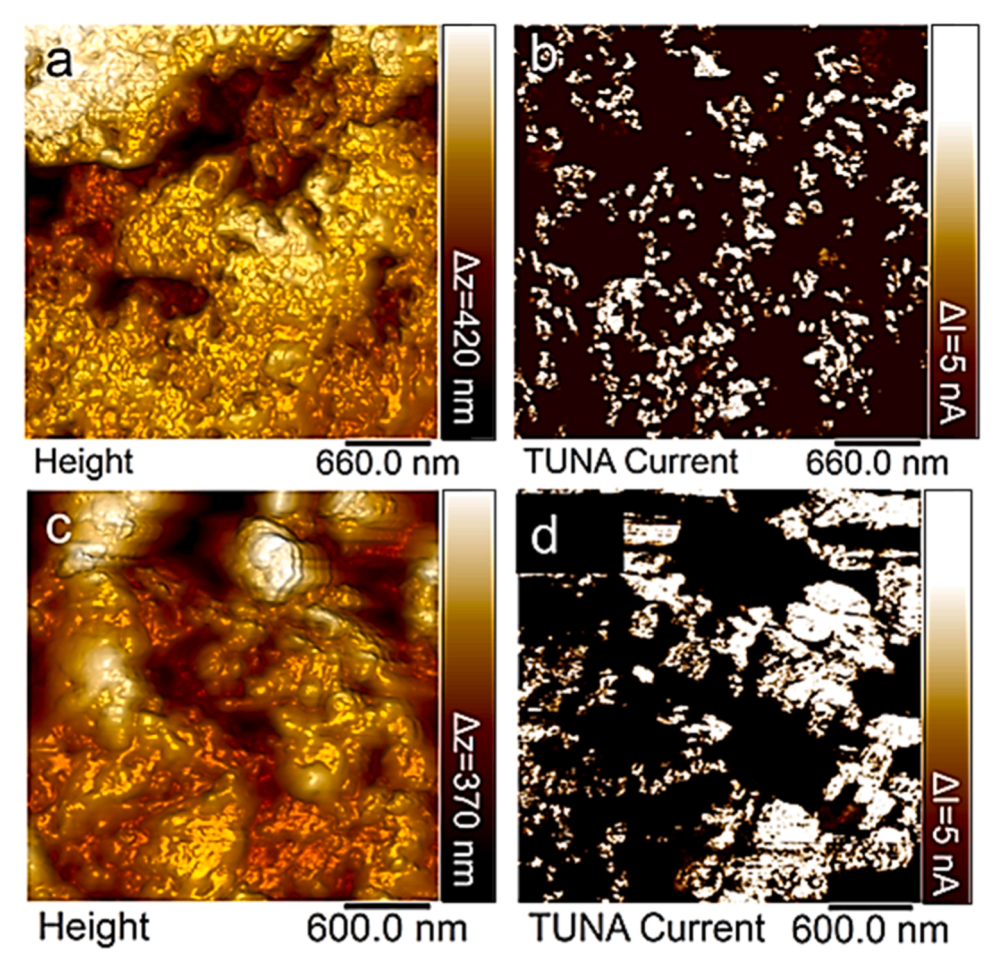


Fig. 7. AFM images of the reduced loaded cell 2 anodes at edge position before operation: a) topography, b) electronic current mapping, after operation: c) topography, and d) electronic current mapping. All measurements were performed at 60 % RH and 1 V bias between tip and sample and image sharpening has been applied.

of Ti in the cathode (Fig. 10b and 10e); (ii) Ti-free interfaces at the membrane/anode side were found but no Ti is detected in the membrane (Fig. 10f and Fig. 11b). Therefore, the Ti deposits probably originate from the Ti bipolar plates of the cathode side. Uncoated Ti-BPP are subject to hydrogen embrittlement. Beside the increase in interface contact resistance of BPPs, Ti corrosion products were released polluting the catalytic layer and membrane [45,49–51]. Using EDX no noble metal could be detected in the membrane.

In Fig. 12, surface potential mappings with a simultaneous determination stiffness using AFM at the edge position close to the anode interface of cell 8 is shown. High potential with low stiffness can be attributed as ionomer while catalyst particles show lower surface potential and higher stiffness [52].

In the stiffness image Fig. 12a) particles or agglomerates with higher stiffness are visible and marked by the red square. At these positions low-potential spots are visible in the membrane (red square; Fig. 12b). Such an area can be assigned to metal particles most likely Ir situated at or directly below the surface close to the anode interface which was not visible with SEM or EDX most likely due to small amounts of noble metals. Such areas were found for cell 2 as well.

To proof these results, the more sensitive XPS analysis (compared to EDX) of the CCM was performed on a diagonal cross-section of cell 2 reaching form the anode catalytic layer into the membrane as indicated in the inset of Fig. 13a).

Carbon in the embedding material in the anode (SI Fig. S6) enabled the possibility to use the C—C signal which corresponds to the C1s peak at 283 eV to detect the position of the electrode/membrane interface in

Fig. 13a). Due to the local resolution of the XPS measurement, a slight blurring in the determination of the positions is to be expected, but a clear trend could be observed so that smaller local deviations are not significant

As visible at the example of cell 2, after operation noble metal was detected within the membrane. Pt was present within the membrane up to the anode interface, and a finite amount of Ir was detected in the membrane close to the anode interface. The high dispersion of Pt within the membrane without pronounced band formation leads to a low local concentration below the detection limit of EDX. Details of the deconvolution of the peaks of Ir and Pt are given in Fig. 13b) and c). It is likely, that Pt and Ir in the membrane are originating from the cathode and anode, respectively. Pt and Ir detachment, dissolution and migration is a well-known degradation mechanism in PEM electrolyzers [15,53–56]

Low-potential areas measured with KPFM without detection of high-stiffness particles indicates an area of a more humid ionomer. A higher hydrophilicity of the ionomer is caused by a degraded ionomer, therefore representing membrane degradation. Such a 15 μ m-wide low-potential area was spotted, without any indication of embedded particles near the cathode interface in the membrane of cell 2.

In Fig. 14a) the topography, in Fig. 14b) the corresponding surface potential image, and in Fig. 14c), a zoomed-in view of the low-potential area are presented.

At this position, the surface potential almost dropped to zero. Similar low potential spots with less extension were also detected at the center of the membrane. In addition, low-potential particles most-likely Pt or Ir particles were found in the membrane at the anode side at different

Electrochimica Acta 542 (2025) 147395

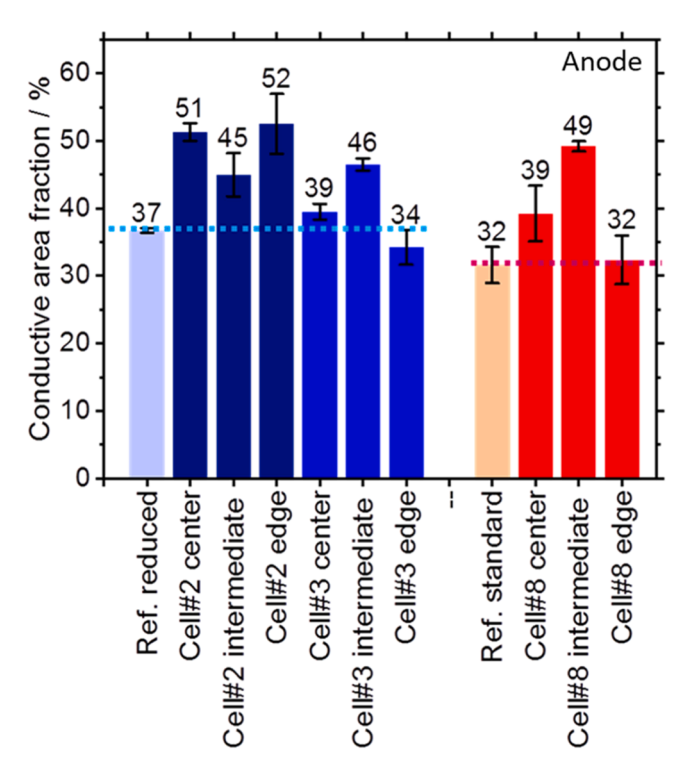


Fig. 8. Conductive area fractions of cross-sections of anodes of three different cells and positions within the CCM before and after operation. The red and blue lines mark the reference values of the pristine samples.

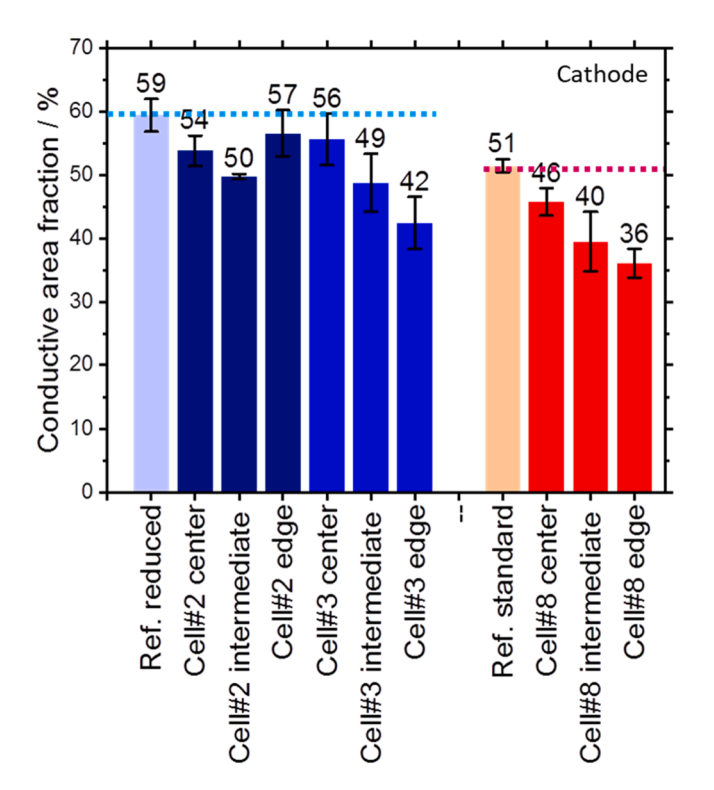


Fig. 9. AFM derived conductive area fractions of all cathodes at different CCM positions, measured at MEA cross-sections before and after operation. The red and blue lines mark the reference values of the pristine samples.

positions of the CCM. In general, no clear trend was observed for the different cells and positions representing degradation phenomena distributed across the whole surface. Additional measurements for cell 8

at different positions as well as for RL reference is shown in SI Fig. S7

Accompanied XPS analysis of the ion exchange resin which accumulates the released ions of the anode cycle can provide a trend of the released F as an indication of ionomer degradation as measured with AFM. In Fig. 15 we could observe an increasing amount of F in the resin during operation but also a decreasing trend in the release rate. These results fit well with the observed trend of decreasing HFR in the electrochemical analysis section. However, both trends indicate that the ionomer degradation slows down during operation time.

The degradation of the membrane measured via AFM and fluorine release most likely results in a thinning of the membrane as the material gets washed out during operation. Therefore, the membrane thickness was measured after finishing the test procedures. In Fig. 16, the membrane thicknesses at the edge positions of the liquid nitrogen freeze-fractured CCMs before and after operation are given for cell 2, cell 3 and cell 8 as well as for the pristine references and an unprocessed N115 membrane. The differences in pristine membrane thickness between RL and SL can be attributed to the manufacturing process, according to the manufacturer. The comparison with the unprocessed N115 membrane shows that the manufacturing, presumably the hot pressing in particular, effects the thickness in general as it decreases from around 123 μ m to 115 μ m and 107 μ m respectively. To draw a conclusive assessment regarding membrane thinning, we obtained the corresponding reference CCMs.

The thickness of the analyzed membranes decreased significantly after operation. Specifically, a decrease of around 9 μm (cell 2 and cell 3) and around 5 μm (cell 8) was observed. Such a decrease in thickness is well-known and reported for electrolysis [22,57,58] and explains the observed improvement in performance during the electrochemical analysis although additional degradation phenomena were detected. We hypothesize that the observed discrepancy between EIS and polarization curve at T4 might be attributed to flooding caused by water drag and membrane thinning which was more pronounce for the polarization curves due to longer stabilization times for the measurements, but further research had to be done to investigate this phenomenon in more detail.

Beside water drag also an increase in gas cross over was measured which can be attributed to the thinning as well. Such a gas cross over can lead to the formation of radicals, which result in chemical degradation of the membrane [30,36,59,60]. The degradation process occurs via an unzipping mechanism driven by the presence of hydrogen peroxide and metal ions, which cannot be completely avoided in such systems [30, 59]. The FRR serves as a measure of membrane degradation and can be influenced by the gas crossover rate [36,59]. In our study, although we observed an increase in crossover, no further increase in FRR was detected. This suggests that, due to the high current density, hydrogen supersaturation had already occurred from the beginning on, causing crossover and membrane degradation [61]. The decrease in FRR over time can likely be attributed to membrane thinning since Marocco et al. reported lower values for the FRR for thinner membranes [59].

In addition, since the fluorine release rate decreased over time critical membrane thinning is unlikely for the used Nafion N115CS membrane. In contrast, although membranes with a thickness of around 50 μm have shown promising results in research [61–63] and a commercial usage would be beneficial to increase the efficiency of electrolyzers such a membrane thinning observed in this study is much more critical. In addition, further obstacles due to the thinner membrane and higher current densities like higher gas crossover [58,63] currently hinder the commercial use.

4. Conclusion

In this work, we analyzed an 8-cell short stack before, during and after approximately 2200 h of operation at high current density by structural in-situ and ex-situ characterization methods. The cell was equipped with two different types of CCMs on with standard and one

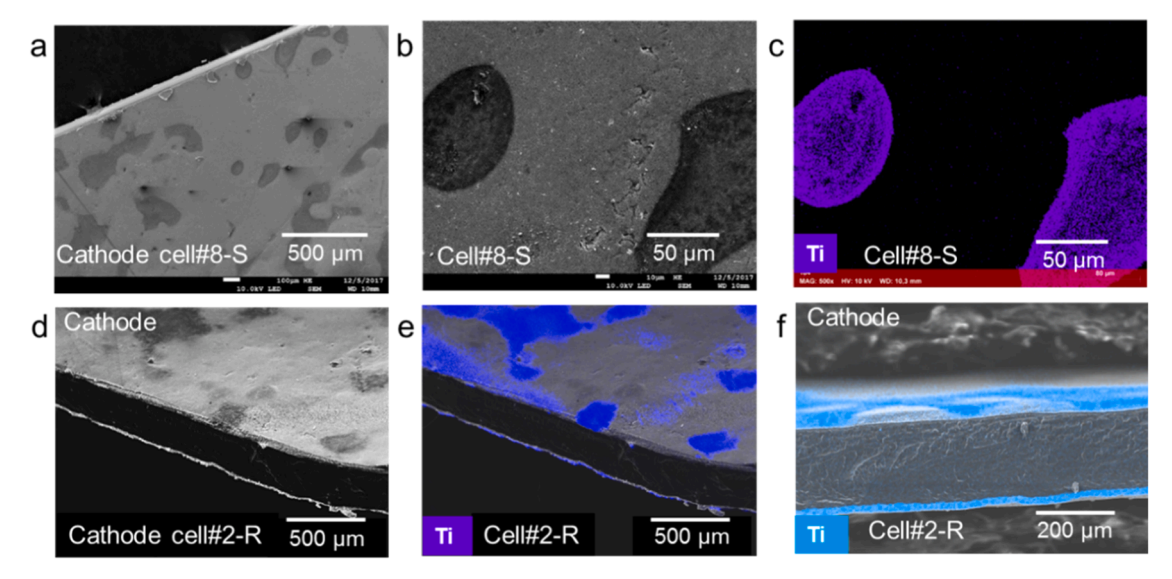


Fig. 10. (a) Large area SEM image of cathode surface of cell 8, (b) magnification of dark areas in (a), (c) corresponding EDX-derived Ti mapping, (d) large area SEM image of cross-section of cell 2 with cathode on top, (e) corresponding SEM image with overlaid Ti mapping, and (f) magnification of cross-section with overlaid Ti mapping.

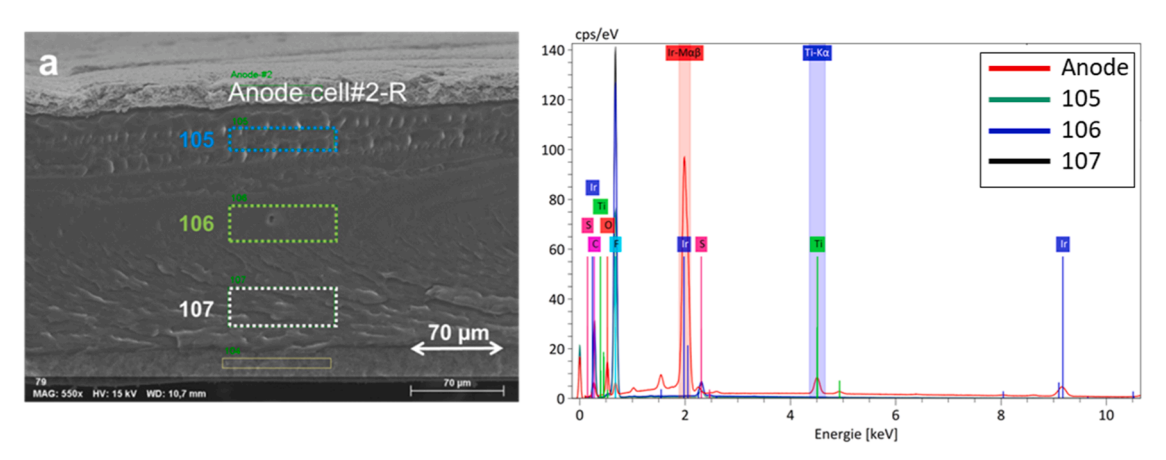


Fig. 11. EDX analysis of cell 2, (a) SEM image with analyzed areas marked, (b) EDX spectra of Ti content in the anode (red) and in the membrane (blue, green).

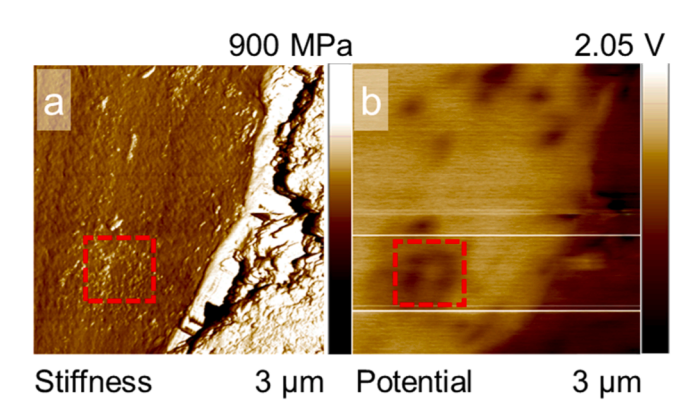


Fig. 12. AFM mappings at edge position in the membrane close the anode interface of cell 8 (a) stiffness, (b) and corresponding potential mapping.

with reduced loading. Electrochemical analysis was done consecutively at different time steps while the physical investigation was done for the pristine and the operated CCMs.

Main observation in this work is the increasing performance during operation. However, this does not imply that there has been no

degradation. In fact, this can be stated as a negative degradation rate caused by membrane thinning, confirmed by AFM, SEM and F release rate, respectively. Thinning of the membrane results in a reduction of ohmic resistances shown by EIS but also increases the permeability of the membrane leading to higher cross over of gases and water which affects the system behavior negatively due to lower gas quality and flooding. In severe scenarios, this can even lead to fatal failure of the stack caused through pinholes. This clearly demonstrates the difficulty in using thinner membranes, which have shown good performances in research, but whose durability must be ensured for commercial applications. Additionally, we observed changes in the conductive area fraction of the anode and the cathode side but contrary. While it is increasing on the anode side it decreases on the cathode side. AFM confirmed the loss of ionomer of the catalytic layer on the anode is more dominant than on the cathode. This demonstrates clearly how the impact of different degradation phenomena can superimpose leading to unexpected results in the performance behavior. Several degradation phenomena were detected like Ti depositions on the cathode. Despite the fact, that these phenomena negatively influence the performance we instead observed an increase performance, highlighting the impact of the membrane thickness. The fact that Ti deposits occur underlines the need for coating the Ti components. At the same time, this also presents an opportunity for cost reduction if stainless steel is used instead of Ti, as

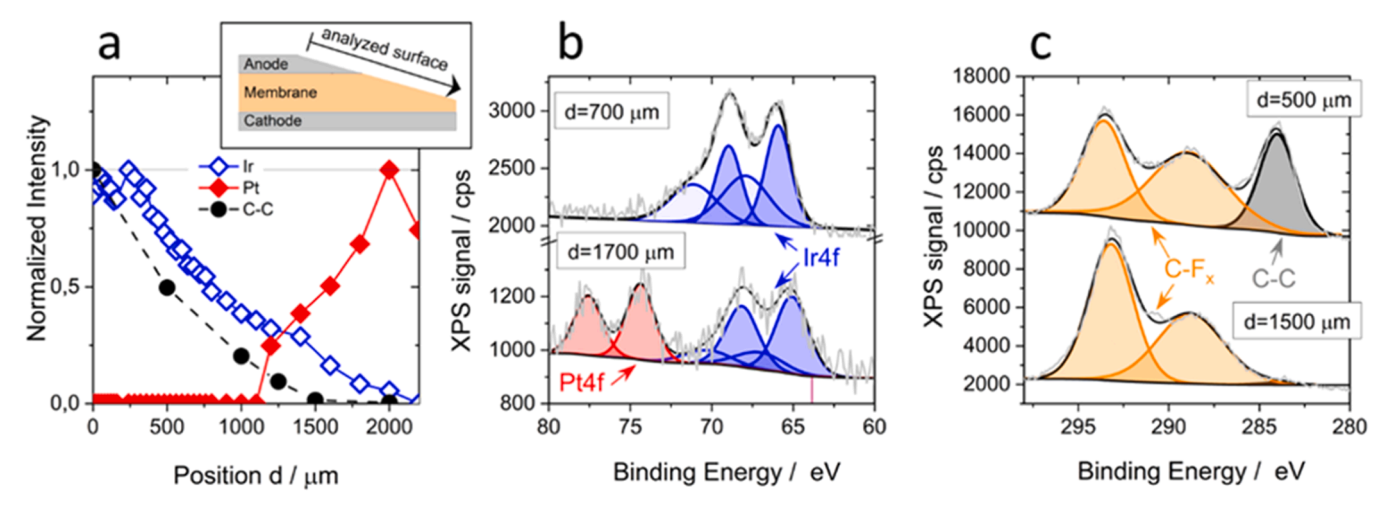


Fig. 13. Results of XPS measurement across cell 2 after operation: (a) intensity profiles of Ir, Pt and C—C, (b) Ir4f and Pt4f peaks at the indicated sample positions, (c) C1s region with signals from carbon support and embedding material (C—C) and ionomer (C-F) at the indicated sample positions.

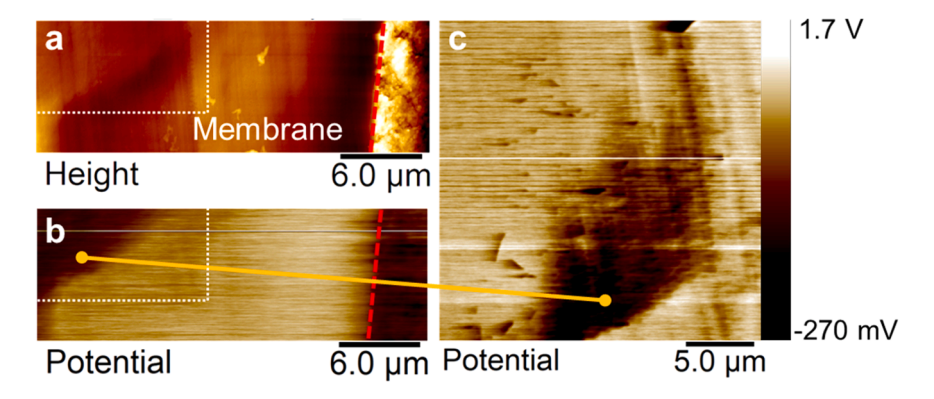


Fig. 14. AFM measurements of the membrane close to the cathode interface of the edge of cell 2, (a) topography, (b) corresponding surface potential mapping, and (c) zoomed-in view on the low-potential area. The red dashed lines in (a) and (b) indicate the boundary between the membrane and electrode.

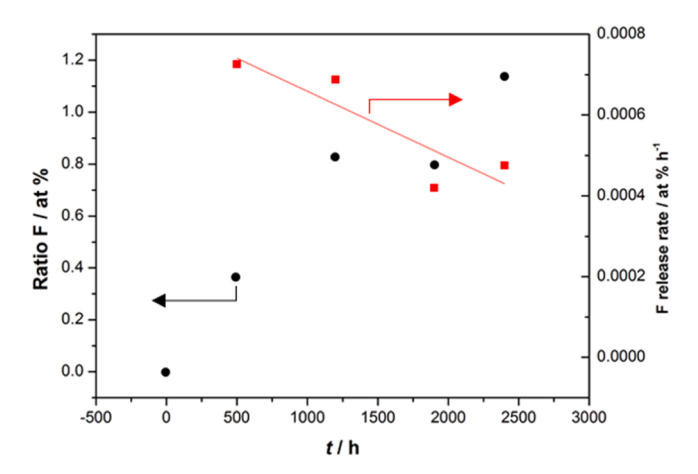


Fig. 15. Time depending ratio of F in at % of the XPS analysis of the ion exchange resin (left) and the calculated F release rate per h. The line indicates the trend of falling release rates.

it can achieve comparable durability with lower costs through appropriate coating [64,65].

Wallnöfer-Orgis et al. summarized typical degradation phenomena and the impact of different operation conditions [47]. As stated, constant stack operation impacts the CCM and the metal BPP/PTL respectively. Dominant phenomena for CCM degradation are chemical

ionomer degradation, chemical carbon degradation, Pt and Ir detachment as well as Ir dissolution [47], which is in good agreement with the phenomena observed in this study. Therefore, high current density can be established as a stressor accelerating similar degradation phenomena that occur under nominal condition. As a stressor it mainly impacts the CCM and should be included in AST protocols to validate the durability of the membrane and catalytic layer.

Synopsis

High current operation of electrolyzer is a promising approach to reduce hydrogen production costs. A deep understanding of degradation mechanism is required to ensure a high lifetime despite high current operation.

Funding

The research leading to these results received funding from the European Union's Seventh Framework Programme (FP7/2007–2013) for the Fuel Cells and Hydrogen Joint Technology Initiative under grant agreement no 621237, "INSIDE- In-situ Diagnostics in Water Electrolyzers".

We also thank the Federal Ministry for Economic Affairs and Energy (BMWi) for financial support of the WESpe project (0325619).

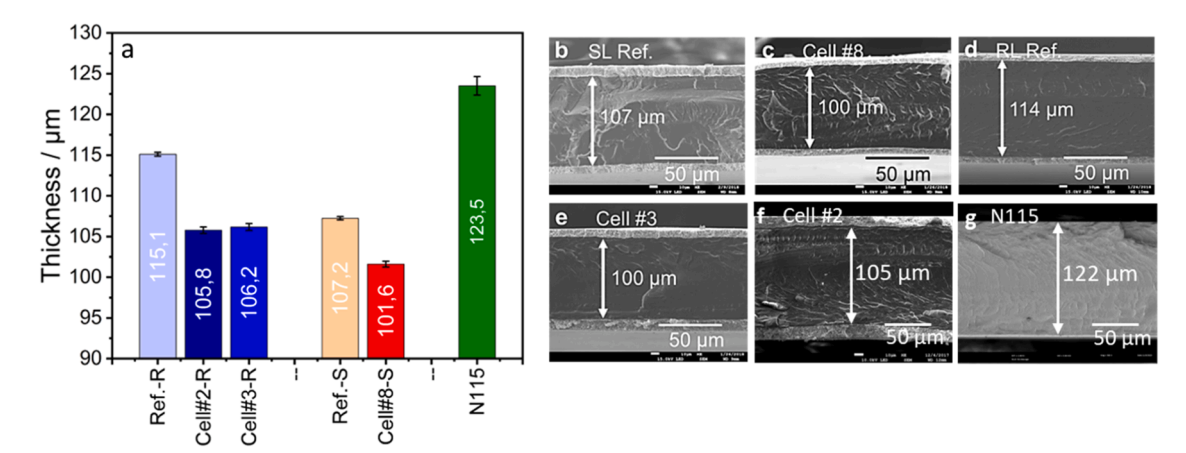


Fig. 16. a) SEM derived membrane thickness measurements of N2-cleaved samples of an unprocessed N115 membrane, pristine references (SL and RL) and cell 2, cell 3, and cell 8 after operation, b) SEM images of N2-cleaved sample of the SL reference with Nafion N115 membrane, c) of cell 8, d) of the RL reference, e) of cell 3, f) of cell2 and (g) of the unprocessed N115 membrane.

Acknowledgment

The authors thank Philipp Lettenmeier for performing the electrochemical measurements of the stack and Suriya Venkatesan for performing the cycling voltammetry (CV) measurements.

CRediT authorship contribution statement

Benjamin Kimmel: Writing – original draft, Investigation, Conceptualization. Tobias Morawietz: Visualization, Investigation. Pawel Gazdzicki: Visualization, Investigation. Aldo S. Gago: Supervision, Conceptualization. K. Andreas Friedrich: Supervision.

Declaration of competing interest

The authors declare that they have no known competing financial interests or personal relationships that could have appeared to influence the work reported in this paper.

Supplementary materials

Supplementary material associated with this article can be found, in the online version, at doi:10.1016/j.electacta.2025.147395.

Data availability

The data that has been used is confidential.

References

- [1] C.J. Barnhart, et al., The energetic implications of curtailing versus storing solarand wind-generated electricity, Energy Environ. Sci. 6 (10) (2013), https://doi. org/10.1039/c3ee41973h
- [2] T. Smolinka, E.T. Ojong, J. Garche, Hydrogen production from renewable energies—electrolyzer technologies, Electrochem. Energy Storage Renew. Sources Grid Balanc. (2015), https://doi.org/10.1016/B978-0-444-62616-5.00008-5.
- [3] M.Z. Jacobson, et al., Impacts of green hydrogen for steel, ammonia, and long-distance transport on the cost of meeting electricity, heat, cold, and hydrogen demand in 145 countries running on 100% wind-water-solar, Smart Energy 11 (2023), https://doi.org/10.1016/j.segy.2023.100106.
- [4] J. El-Kadi, et al., The potential of green ammonia in the de-fossilization of the steel, glass and cement industries, Philos. Trans. Math. Phys. Eng. Sci. 382 (2282) (2024) 20230270. https://doi.org/10.1098/rsta.2023.0270.
- [5] T. Wang, X. Cao, L. Jiao, PEM water electrolysis for hydrogen production: fundamentals, advances, and prospects, Carbon Neutrality 1 (1) (2022), https://doi.org/10.1007/s43979-022-00022-8.
- [6] Z. Abdin, et al., A review of renewable hydrogen hybrid energy systems towards a sustainable energy value chain, Sustain. Energy Fuels 7 (9) (2023) 2042–2062, https://doi.org/10.1039/d3se00099k.

- [7] M. Arunachalam, D.S. Han, Efficient solar-powered PEM electrolysis for sustainable hydrogen production: an integrated approach, Emergent. Mater. 7 (4) (2024) 1401–1415, https://doi.org/10.1007/s42247-024-00697-y.
- [8] J. Lei, et al., A comprehensive review on the power supply system of hydrogen production electrolyzers for future integrated energy systems, Energies (Basel) 17 (4) (2024). https://doi.org/10.3390/en17040935.
- [9] P. Shirvanian, F. van Berkel, Novel components in Proton Exchange Membrane (PEM) water Electrolyzers (PEMWE): status, challenges and future needs. a mini review, Electrochem. Commun. 114 (2020), https://doi.org/10.1016/j. elecom 2020 106704
- [10] P. Lettenmeier, et al., Durable membrane electrode assemblies for Proton exchange membrane electrolyzer systems operating at high current densities, Electrochim. Acta 210 (2016) 502–511, https://doi.org/10.1016/j.electacta.2016.04.164.
- [11] A. Albert, et al., Stability and degradation mechanisms of radiation-grafted polymer electrolyte membranes for water electrolysis, ACS Appl. Mater. Interfaces 8 (24) (2016) 15297–15306, https://doi.org/10.1021/acsami.6b03050.
- [12] E. Kuhnert, et al., A review of accelerated stress tests for enhancing MEA durability in PEM water electrolysis cells, Int. J. Energy Res. 2023 (2023) 1–23, https://doi. org/10.1155/2023/3183108.
- [13] S. Cherevko, et al., Stability of nanostructured iridium oxide electrocatalysts during oxygen evolution reaction in acidic environment, Electrochem. Commun. 48 (2014) 81–85, https://doi.org/10.1016/j.elecom.2014.08.027.
- [14] C. Spöri, et al., The stability challenges of oxygen evolving electrocatalysts: towards a common fundamental understanding and mitigation of catalyst degradation, Angew. Chem. 129 (22) (2017) 6088–6117, https://doi.org/ 10.1002/ange.201608601.
- [15] H. Yu, et al., Microscopic insights on the degradation of a PEM water electrolyzer with ultra-low catalyst loading, Appl. Catal. B: Environ. 260 (2020), https://doi. org/10.1016/j.apcatb.2019.118194.
- [16] A. Weiß, et al., Impact of intermittent operation on lifetime and performance of a PEM water electrolyzer, J. Electrochem. Soc. 166 (8) (2019) F487–F497, https://doi.org/10.1149/2.0421908jes.
- [17] S.M. Alia, Current research in low temperature proton exchange membrane-based electrolysis and a necessary shift in focus, Curr. Opin. Chem. Eng. 33 (2021), https://doi.org/10.1016/j.coche.2021.100703.
- [18] S.M. Alia, S. Stariha, R.L. Borup, Electrolyzer durability at low catalyst loading and with dynamic operation, J. Electrochem. Soc. 166 (15) (2019) F1164–F1172, https://doi.org/10.1149/2.0231915jes.
- [19] C. Liu, et al., Degradation effects at the porous transport layer/catalyst layer interface in polymer electrolyte membrane water electrolyzer, J. Electrochem. Soc. 170 (3) (2023), https://doi.org/10.1149/1945-7111/acc1a5.
- [20] F.N. Khatib, et al., Material degradation of components in polymer electrolyte membrane (PEM) electrolytic cell and mitigation mechanisms: a review, Renew. Sustain. Energy Rev. 111 (2019) 1–14, https://doi.org/10.1016/j. proc. 2010.05.007
- [21] B. Kimmel, et al., Investigation of the degradation phenomena of a proton exchange membrane electrolyzer stack by successive replacement of aged components in single cells, ACS Sustain. Chem. Eng. 13 (11) (2025) 4330–4340, https://doi.org/10.1021/acssuschemeng.4c07358.
- [22] M. Chandesris, et al., Membrane degradation in PEM water electrolyzer: numerical modeling and experimental evidence of the influence of temperature and current density, Int. J. Hydrogen. Energy 40 (3) (2015) 1353–1366, https://doi.org/ 10.1016/j.ijhydene.2014.11.111.
- [23] F. Fouda-Onana, et al., Investigation on the degradation of MEAs for PEM water electrolysers part I: effects of testing conditions on MEA performances and membrane properties, Int. J. Hydrogen. Energy 41 (38) (2016) 16627–16636, https://doi.org/10.1016/j.ijhydene.2016.07.125.
- [24] T. Morawietz, et al., High-resolution analysis of ionomer loss in catalytic layers after operation, J. Electrochem. Soc. 165 (6) (2018) F3139–F3147, https://doi. org/10.1149/2.0151806jes.

- [25] P. Millet, et al., Cell failure mechanisms in PEM water electrolyzers, Int. J. Hydrogen. Energy 37 (22) (2012) 17478–17487, https://doi.org/10.1016/j. iihydene 2012.06.017
- [26] C. Rakousky, et al., An analysis of degradation phenomena in polymer electrolyte membrane water electrolysis, J. Power. Sources 326 (2016) 120–128, https://doi. org/10.1016/j.jpowsour.2016.06.082.
- [27] S. Sun, et al., Investigations on degradation of the long-term proton exchange membrane water electrolysis stack, J. Power. Sources 267 (2014) 515–520, https://doi.org/10.1016/j.jpowsour.2014.05.117.
- [28] X.-Z. Yuan, et al., Degradation of a PEM fuel cell stack with Nafion® membranes of different thicknesses. Part II: ex situ diagnosis, J. Power. Sources 205 (2012) 324–334, https://doi.org/10.1016/j.jpowsour.2012.01.074.
- [29] B. Kimmel, et al., Opportunities of in situ diagnostics and current distribution in proton exchange membrane water electrolyzers with segmented bipolar plates, Appl. Energy 380 (2025), https://doi.org/10.1016/j.apenergy.2024.125106.
- [30] Q. Feng, et al., A review of proton exchange membrane water electrolysis on degradation mechanisms and mitigation strategies, J. Power. Sources 366 (2017) 33–55, https://doi.org/10.1016/j.jpowsour.2017.09.006.
- [31] S. Yuan, et al., Rational electrode design for low-cost proton exchange membrane water electrolyzers, Cell Rep. Phys. Sci. 5 (3) (2024), https://doi.org/10.1016/j. xcrp.2024.101880.
- [32] S. Krishnan, et al., Present and future cost of alkaline and PEM electrolyser stacks, Int. J. Hydrogen. Energy 48 (83) (2023) 32313–32330, https://doi.org/10.1016/j. iihvdene.2023.05.031.
- [33] F.J. Hackemüller, et al., Manufacturing of large-scale titanium-based porous transport layers for polymer electrolyte membrane electrolysis by tape casting, Adv. Eng. Mater. 21 (6) (2019), https://doi.org/10.1002/adem.201801201.
- [34] X. Wang, A.G. Star, R.K. Ahluwalia, Performance of Polymer electrolyte membrane water electrolysis systems: configuration, stack materials, turndown and efficiency, Energies (Basel) 16 (13) (2023), https://doi.org/10.3390/en16134964.
- [35] M. Kisti, et al., Recent advances in polymer electrolyte membrane water electrolyzer stack development studies: a review, ACS Omega 10 (10) (2025) 9824–9853, https://doi.org/10.1021/acsomega.4c10147.
- [36] E. Kuhnert, et al., Analysis of PEM water electrolyzer failure due to induced hydrogen crossover in catalyst-coated PFSA membranes, Membranes (Basel) 13 (3) (2023), https://doi.org/10.3390/membranes13030348.
- [37] K.E. Ayers, et al., Pathways to ultra-low platinum group metal catalyst loading in proton exchange membrane electrolyzers, Catal. Today 262 (2016) 121–132, https://doi.org/10.1016/j.cattod.2015.10.019.
- [38] T. Malkow, G. De Marco, G. Tsotridis, EU Harmonised Cyclic Voltammetry Test Method For Low-Temperature Water Electrolysis Single Cells, Publications Office of the European Union, 2018. https://doi.org/10.2760/140687.
- [39] J.M. Rheaume, B. Müller, M. Schulze, XPS analysis of carbon-supported platinum electrodes and characterization of CO oxidation on PEM fuel cell anodes by electrochemical half cell methods, J. Power. Sources 76 (1) (1998) 60–68, https:// doi.org/10.1016/s0378-7753(98)00141-4.
- [40] L. Wang, et al., Nanostructured Ir-supported on Ti4O7 as a cost-effective anode for proton exchange membrane (PEM) electrolyzers, Phys. Chem. Chem. Phys. 18 (6) (2016) 4487–4495, https://doi.org/10.1039/c5cp05296c.
- [41] P. Lettenmeier, et al., Nanosized IrOx-Ir catalyst with relevant activity for anodes of proton exchange membrane electrolysis produced by a cost-effective procedure, Angew. Chem. 128 (2) (2015) 752–756, https://doi.org/10.1002/ ange.201507626
- [42] P. Jovanovic, et al., Electrochemical dissolution of iridium and iridium oxide particles in acidic Media: transmission electron microscopy, Electrochemical flow cell coupled to inductively coupled plasma mass spectrometry, and X-ray absorption spectroscopy study, J. Am. Chem. Soc. 139 (36) (2017) 12837–12846, https://doi.org/10.1021/jacs.7b08071.
- [43] T. Lagarteira, et al., Highly active screen-printed Ir Ti407 anodes for proton exchange membrane electrolyzers, Int. J. Hydrogen. Energy 43 (35) (2018) 16824–16833, https://doi.org/10.1016/j.ijhydene.2018.02.179.
- [44] J. Cho, et al., Dissolution of the Ti porous transport layer in proton exchange membrane water electrolyzers, J. Mater. Chem. A 12 (35) (2024) 23688–23696, https://doi.org/10.1039/d4ta02755h.

- [45] S. Bin, et al., High-pressure proton exchange membrane water electrolysis: current status and challenges in hydrogen production, Int. J. Hydrogen. Energy 67 (2024) 390–405, https://doi.org/10.1016/j.ijhydene.2024.04.188.
- [46] K. Ayers, et al., PEM electrolysis, a forerunner for clean hydrogen, Electrochem. Soc. Interface 30 (4) (2021) 67–72, https://doi.org/10.1149/2.F16214if.
- [47] E. Wallnöfer-Ogris, et al., A review on understanding and identifying degradation mechanisms in PEM water electrolysis cells: insights for stack application, development, and research, Int. J. Hydrogen. Energy 65 (2024) 381–397, https:// doi.org/10.1016/i.iihvdene.2024.04.017.
- [48] C. Rakousky, et al., Polymer electrolyte membrane water electrolysis: restraining degradation in the presence of fluctuating power, J. Power. Sources 342 (2017) 38–47, https://doi.org/10.1016/j.jpowsour.2016.11.118.
- [49] A.S. Gago, et al., Protective coatings on stainless steel bipolar plates for proton exchange membrane (PEM) electrolysers, J. Power. Sources 307 (2016) 815–825, https://doi.org/10.1016/j.jpowsour.2015.12.071.
- [50] A. Baroutaji, et al., Additive manufacturing for proton exchange membrane (PEM) hydrogen technologies: merits, challenges, and prospects, Int. J. Hydrogen. Energy 52 (2024) 561–584, https://doi.org/10.1016/j.ijhydene.2023.07.033.
- [51] K.W. Ahmed, et al., Effect of components and operating conditions on the performance of PEM electrolyzers: a review, Electrochem 3 (4) (2022) 581–612, https://doi.org/10.3390/electrochem3040040.
- [52] T. Morawietz, et al., Membranes, electrodes, and membrane-electrodes assemblies analyzed before and after operation by atomic force microscopy, ECS Trans. 68 (3) (2015) 3–12, https://doi.org/10.1149/06803.0003ecst.
- [53] J. Dodwell, et al., Open-circuit dissolution of platinum from the cathode in polymer electrolyte membrane water electrolysers, J. Power. Sources 498 (2021), https://doi.org/10.1016/j.jpowsour.2021.229937.
- [54] A.P. Dam, et al., Catalyst dissolution in PEM water electrolysis: influence of time, current density and iridium ion transport in single-pass and recirculation water flow modes, Appl. Catal. B: Environ. Energy 365 (2025), https://doi.org/10.1016/j.apcatb.2024.124946.
- [55] H.S. Oh, et al., Electrochemical catalyst-support effects and their stabilizing role for IrOx nanoparticle catalysts during the oxygen evolution reaction, J. Am. Chem. Soc. 138 (38) (2016) 12552–12563, https://doi.org/10.1021/jacs.6b07199.
- [56] S. Cherevko, et al., Oxygen evolution activity and stability of iridium in acidic media. Part 1. – metallic iridium, J. Electroanal. Chem. 773 (2016) 69–78, https://doi.org/10.1016/j.jelechem.2016.04.033.
- [57] S. Siracusano, et al., Degradation issues of PEM electrolysis MEAs, Renew. Energy 123 (2018) 52–57, https://doi.org/10.1016/j.renene.2018.02.024.
- [58] S.H. Frensch, et al., Influence of the operation mode on PEM water electrolysis degradation, Int. J. Hydrogen. Energy 44 (57) (2019) 29889–29898, https://doi. org/10.1016/j.ijhydene.2019.09.169.
- [59] P. Marocco, et al., Online measurements of fluoride ions in proton exchange membrane water electrolysis through ion chromatography, J. Power. Sources (2021) 483, https://doi.org/10.1016/j.jpowsour.2020.229179.
- [60] S.H. Frensch, et al., Impact of iron and hydrogen peroxide on membrane degradation for polymer electrolyte membrane water electrolysis: computational and experimental investigation on fluoride emission, J. Power. Sources 420 (2019) 54–62, https://doi.org/10.1016/j.jpowsour.2019.02.076.
- [61] M. Bernt, et al., Analysis of gas permeation phenomena in a PEM water electrolyzer operated at high pressure and high current density, J. Electrochem. Soc. 167 (12) (2020), https://doi.org/10.1149/1945-7111/abaa68.
- [62] H.R. Corti, Polymer electrolytes for low and high temperature PEM electrolyzers, Curr. Opin. Electrochem. 36 (2022), https://doi.org/10.1016/j. coelec.2022.101109.
- [63] A. Martin, et al., Hydrogen crossover in PEM water electrolysis at current densities up to 10 A cm-2, J. Electrochem. Soc. 169 (9) (2022), https://doi.org/10.1149/ 1945-7111/ac908c.
- [64] S. Stiber, et al., Long-term operation of Nb-coated stainless steel bipolar plates for proton exchange membrane water electrolyzers, Adv. Energy Sustain. Res. 3 (8) (2022), https://doi.org/10.1002/aesr.202200024.
- [65] S. Stiber, et al., A high-performance, durable and low-cost proton exchange membrane electrolyser with stainless steel components, Energy Environ. Sci. 15 (1) (2022) 109–122, https://doi.org/10.1039/d1ee02112e.